ATLAS CONF Note

ATLAS-CONF-2020-017

2nd June 2020

Measurement of the dijet momentum balance in Pb+Pb and pp collisions at $\sqrt{s_{\mathrm{NN}}}$ = 5.02 TeV with the ATLAS detector

The ATLAS Collaboration

This note presents measurements of the dijet momentum balance of anti-k_t $R = 0.4$ jets at center-of-mass energy $\sqrt{s_{\mathrm{NN}}}$ = 5.02 TeV in Pb+Pb and pp collisions by the ATLAS experiment. The measurement was performed using 1.72 nb^{-1} of Pb+Pb data and 260 pb^{-1} of pp data collected in 2018 and 2017 respectively. This note presents distributions of the unfolded $\frac{1}{\mathrm{N_{pair}}}\frac{\mathrm{dN_{pair}}}{\mathrm{d}x_{\mathrm{J}}}$, where x_{J} is the ratio of the transverse momentum (p_{T}) of the subleading jet to the leading jet, as a function of the p_{T} of the leading jet and of collision centrality. In pp collisions the x_{J} distributions reach a maximum at $x_{\mathrm{J}} \approx 1$ and decrease approximately linearly with decreasing x_{J}. In central Pb+Pb collisions for leading jets with $158 < p_{\mathrm{T}} < 200$ GeV, the x_{J} distributions are approximately constant for $x_{\mathrm{J}} > 0.5$. Even at the highest leading jet p_{T} measured, $398 < p_{\mathrm{T}} < 562$ GeV, significant modification from the shape in pp collisions is observed. These measurements are compared with previous measurements at $\sqrt{s_{\mathrm{NN}}}$ = 2.76 TeV and are found to agree within the systematic uncertainties. These results will help in understanding the strength and mechanism for jet modifications in the quark-gluon plasma.

ATLAS-CONF-2020-017
09 June 2020

1 Introduction

The primary physics aim of the heavy-ion program at the Large Hadron Collider (LHC) is to produce and study the quark-gluon plasma (QGP), the high-temperature state of quantum-chromodynamics (QCD) matter in which quarks and gluons are no longer confined within protons and neutrons (for a recent review see Ref. [1]). Measurements of jets in heavy-ion collisions provide information about the short distance scale interactions of high energy partons with the QGP. The overall rate of jets at a given transverse momentum, p_{T}, in Pb+Pb collisions is found to be reduced by approximately a factor of two compared to expectations based on pp collisions scaled by the increased partonic luminosity in Pb+Pb collisions, as demonstrated in the measurement of the nuclear modification factor in Ref. [2]. This suppression is observed to persist to the highest transverse momenta measured in Ref. [2], approximately 1 TeV. The mechanism for the observed suppression is thought to be the loss of energy outside the jet cone via interactions of the jet constituents with the QGP [1, 3].

Pairs of jets have been found to have an enhanced probability to being momentum-imbalanced in Pb+Pb collisions compared to pp collisions [4–6]. The interpretation of these results is that the lower momentum, sub-leading, jet loses more energy than the higher momentum, leading, jet. The unequal energy loss of the jets in a dijet pair is thought to arise from unequal path lengths through the QGP depending on the geometry of the collision and the orientation of the jet trajectories [7]. Because this observable has two jets, which are both expected to lose some amount of energy, it can provide different sensitivity to the path length dependence of energy loss than single jet suppression and photon-jet balance. It is therefore of interest to have measurements of the dijet momentum balance covering as much of the kinematic range of the single jet measurements as possible.

First measurements of the dijet momentum imbalance were not unfolded for detector resolution [4, 5]. A later measurement from ATLAS at $\sqrt{s_{\mathrm{NN}}}$ =2.76 TeV included a two-dimensional Bayesian unfolding to correct for detector resolution [6]. The momentum balance distributions in Pb+Pb collisions are observed to become more similar to those in pp collisions with increasing leading-jet p_{T}. However, due to the limited luminosity (0.14 nb^{-1}) the highest leading-jet p_{T} selection available in Ref. [6] includes all jets with $p_{\mathrm{T}} > 200$ GeV hence the detailed high-p_{T} behavior of this observable is currently unknown.

This measurement extends the measurement of the dijet momentum balance to $\sqrt{s_{\mathrm{NN}}} = 5.02$ TeV and uses 1.72 nb^{-1} of Pb+Pb data collected in 2018 to extend the reach of this measurement to leading jets with $398 < p_{\mathrm{T}} < 562$ GeV. For comparison, 260 pb^{-1} of pp data at the same collision energy is used. Jets are reconstructed using the anti-k_t [8] algorithm with a radius parameter of $R = 0.4$. As in Ref. [6], the variable of interest is the transverse momentum balance of back-to-back in azimuth[1] jets with $|\Delta\phi| \equiv |\phi_1 - \phi_2| > \frac{7\pi}{8}$. The subscripts 1 and 2 refer to the leading and sub-leading jet, respectively. The momentum balance is defined in Equation 1:

$$x_{\mathrm{J}} = \frac{p_{\mathrm{T},2}}{p_{\mathrm{T},1}} \tag{1}$$

With the direct observable in this measurement being the dijet yield normalized by the number of jet pairs in a given $p_{\mathrm{T},1}$ region, $\frac{1}{\mathrm{N_{pair}}}\frac{\mathrm{dN_{pair}}}{\mathrm{d}x_{\mathrm{J}}}$. This measurement is quoted for $p_{\mathrm{T},1}$between 158 and 562 GeV for jets with $|\eta| < 2.1$.

[1] ATLAS uses a right-handed coordinate system with its origin at the nominal interaction point (IP) in the center of the detector and the z-axis along the beam pipe. The x-axis points from the IP to the center of the LHC ring, and the y-axis points upwards. Cylindrical coordinates (r, ϕ) are used in the transverse plane, ϕ being the azimuthal angle around the z-axis. The pseudorapidity is defined in terms of the polar angle θ as $\eta = -\ln\tan(\theta/2)$. Angular distance is measured in units of $\Delta R \equiv \sqrt{(\Delta\eta)^2 + (\Delta\phi)^2}$.

2 ATLAS detector

The ATLAS detector [9] at the LHC covers nearly the entire solid angle around the collision point. It consists of an inner tracking detector surrounded by a thin superconducting solenoid, electromagnetic and hadronic calorimeters, a zero-degree calorimeter, and a muon spectrometer incorporating three large superconducting toroidal magnets. The inner-detector system is immersed in a 2 T axial magnetic field and provides charged particle tracking in the range $|\eta| < 2.5$.

The high-granularity silicon pixel detector covers the vertex region and typically provides four measurements per track, the first hit being normally in the innermost layer. It is followed by the silicon microstrip tracker which usually provides four two-dimensional measurement points per track. These silicon detectors are complemented by the transition radiation tracker, which enables radially extended track reconstruction up to $|\eta| = 2.0$.

The calorimeter system covers the pseudorapidity range $|\eta| < 4.9$. Within the region $|\eta| < 3.2$, electromagnetic calorimetry is provided by barrel and endcap high-granularity lead/liquid-argon (LAr) electromagnetic calorimeters, with an additional thin LAr presampler covering $|\eta| < 1.8$, to correct for energy loss in material upstream of the calorimeters. Hadronic calorimetry is provided by the steel/scintillating-tile calorimeter, segmented into three barrel structures within $|\eta| < 1.7$, and two copper/LAr hadronic endcap calorimeters. The solid angle coverage is completed with forward copper/LAr and tungsten/LAr calorimeter modules optimized for electromagnetic and hadronic measurements respectively.

The zero-degree calorimeters (ZDCs) are located symmetrically at z = ±140 m and cover $|\eta| > 8.3$. They are constructed from tungsten absorber plates, while Čerenkov light is transmitted via quartz fibers. In Pb+Pb collisions the ZDCs primarily measure "spectator" neutrons, which are neutrons that do not interact hadronically when the incident nuclei collide. A ZDC coincidence trigger is implemented by requiring the pulse height from each ZDC to be above a threshold set to accept the single-neutron peak.

A two-level trigger system is used to select interesting events [10]. The Level-1 trigger is implemented in hardware and uses a subset of detector information, including ZDC coincidence, to reduce the event rate to a design value of at most 100 kHz. This is followed by a software-based trigger level which reduces the event rate to several kHz.

3 Event and data selection

All events included in this analysis are required to contain at least one reconstructed vertex as well as to satisfy detector and data-quality requirements. These events are additionally required to have been selected by a jet trigger and have the leading jet in a region where the trigger is fully efficient. Although only a small fraction of Pb+Pb events (< 0.5%) contain multiple collisions, the anti-correlation between the total transverse energy deposited in the forward calorimeter, $\Sigma E_{\mathrm{T}}^{\mathrm{FCal}}$, and the number of neutrons measured in the ZDC is used to suppress these events.

The overlap area of two colliding nuclei in Pb+Pb collisions is characterized by the total transverse energy deposited in the FCal [11]. This analysis uses five centrality intervals which are defined according to successive percentiles of the $\Sigma E_{\mathrm{T}}^{\mathrm{FCal}}$ distribution obtained in Minimum Bias collisions. The centrality regions used in this analysis, starting at the most central (largest $\Sigma E_{\mathrm{T}}^{\mathrm{FCal}}$) to peripheral (lowest $\Sigma E_{\mathrm{T}}^{\mathrm{FCal}}$) collisions are: 0-10%, 10-20%, 20-40%, 40-60%, and 60-80%.

This analysis uses two Monte Carlo (MC) samples to evaluate the performance of the detector and analysis procedure, and to correct the measured distributions for detector effects. The pp MC used in this analysis includes 32×10^6 Pythia8 [12] pp jet events at $\sqrt{s} = 5.02$ TeV with the A14 ATLAS tune [13] and the NNPDF23LO parton distribution functions (PDFs) [14]. Pileup from additional pp collisions is generated by Pythia8, with parameter values set to the A3 tune [15] and using NNPDF23LO, with a distribution of the number of extra collisions matching that of data. The Pb+Pb MC sample uses 32×10^6 pp Pythia8 events with the same tune and PDFs as in pp MC samples that are overlayed on top of events from a dedicated sample of Pb+Pb data events. This sample was recorded with a combination of minimum bias trigger and total energy triggers to enhance the statistics in central collisions. This "MC overlay" sample was reweighted on an event-by-event basis such that it has the same centrality distribution as the jet-triggered data sample. The detector response in all MC samples was simulated using Geant4 [16, 17].

4 Jet Reconstruction and Analysis

Similar to previous ATLAS jet measurements [2] in Pb+Pb collisions, the jets were reconstructed using the anti-k_t algorithm [8] as implemented in the FastJet software package [18]. The jets were reconstructed with radius parameter $R = 0.4$ by clustering calorimetric "towers" of spatial size $\Delta\eta \times \Delta\phi = 0.1 \times \frac{\pi}{32}$. A background subtraction procedure was applied which uses the underlying event (UE) average transverse energy density, $\rho(\eta, \phi)$, where the ϕ dependence accounts for azimuthal anisotropy due to correlations in particle production caused by flow [19]. The UE estimation is additionally corrected for η and ϕ dependent non-uniformities of the detector. The jet reconstruction in pp collisions follows the same procedure as in heavy-ion collisions but without UE corrections for the η and ϕ variations in the detector response, as well as without azimuthal modulation of the UE.

The performance of the reconstruction of jets is characterized by evaluating the jet energy scale (JES) and jet energy resolution (JER), which corresponds to the mean and variance of the $p_{\mathrm{T}}^{\mathrm{reco}}/p_{\mathrm{T}}^{\mathrm{truth}}$ distribution where $p_{\mathrm{T}}^{\mathrm{reco}}$ is the reconstructed jet p_{T} and $p_{\mathrm{T}}^{\mathrm{truth}}$ is the p_{T} of the matched generator-level jet, within $\Delta R < 0.3$. Generator-level jets are built from particle four-vectors obtained from the MC generator and are defined by applying the anti-k_t algorithm with radius parameter $R = 0.4$ to stable particles with a proper lifetime greater than 30 ps, but excluding muons and neutrinos. Figure 1 shows the JES and the JER as a function of $p_{\mathrm{T}}^{\mathrm{truth}}$ for Pb+Pb and pp collisions. The JES deviates from unity by up to 1.5% for 0-10% central Pb+Pb and up to 0.5% in pp collisions. The deviation from unity in the JES for pp collisions arises from the application of a strong isolation cut in the calibration procedure which cannot be applied as part of this analysis. Due to the underlying event fluctuations in Pb+Pb collisions the JER degrades in central Pb+Pb collisions. The jet reconstruction efficiency is evaluated as the probability of a jet to be reconstructed with a p_{T} larger than 44 GeV. Figure 2 shows that the jet reconstruction efficiency is greater than 90% (70%) in pp (central Pb+Pb) collisions for $p_{\mathrm{T}}^{\mathrm{truth}} > 50$ GeV.

This analysis considers the measured leading dijet pair constructed from the two highest p_{T} jets in the event with reconstructed $p_{\mathrm{T},1} > 79$ GeV, $p_{\mathrm{T},2} > 44$ GeV and $|\eta| < 2.1$. The dijets are required to be back to back in azimuth through requiring $|\Delta\phi| > 7\pi/8$. For these dijet pairs the symmetrized two-dimensional ($p_{\mathrm{T},1}$,$p_{\mathrm{T},2}$) distributions are measured. These distributions contain both the dijet signal as well as combinatoric contributions from uncorrelated jets. The contribution from combinatoric jets is estimated and subtracted by measuring the symmetrized two-dimensional ($p_{\mathrm{T},1}$,$p_{\mathrm{T},2}$) distribution of dijets within $1 < |\Delta\phi| < 1.4$ and

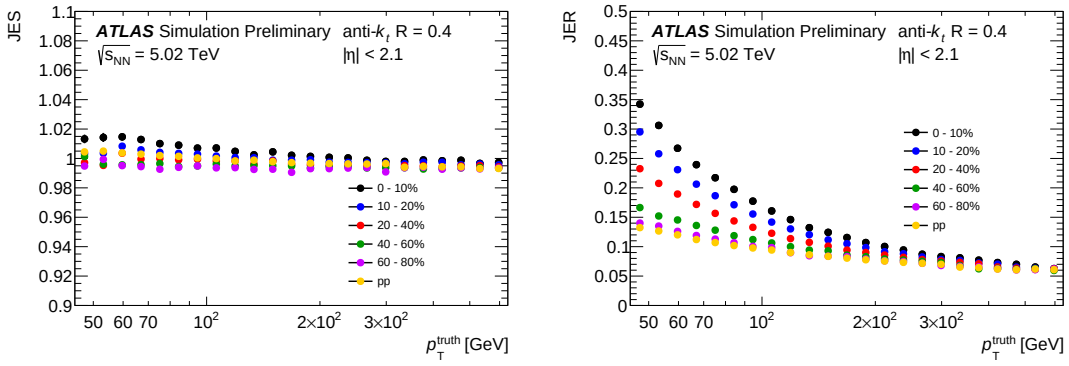

Figure 1: The JES (left) and JER (right) as a function of $p_{\mathrm{T}}^{\mathrm{truth}}$ in Pb+Pb and in pp collisions.

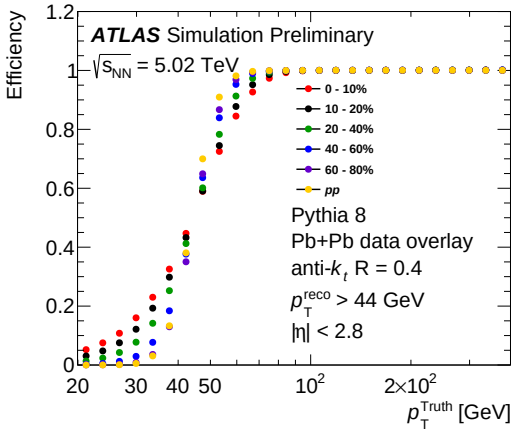

Figure 2: The efficiency for reconstructing jets as a function of $p_{\mathrm{T}}^{\mathrm{truth}}$ for jets reconstructed with $p_{\mathrm{T}}^{\mathrm{reco}} > 44$ GeV for Pb+Pb collisions with the centrality selections: 0–10%, 10–20%, 20–40%, 40–60%, 60–80%.

normalizing to the $\Delta\phi$ window of the measurement region, assuming a flat $\Delta\phi$ distribution of uncorrelated jets. In the kinematic range of this measurement the combinatoric background contribution is small.

The measured ($p_{\mathrm{T},1}$,$p_{\mathrm{T},2}$) distributions are unfolded for detector effects using the iterative Bayesian unfolding [20] procedure implemented in the RooUnfold [21] software package. The unfolding in this measurement is done on the two-dimensional ($p_{\mathrm{T},1}$,$p_{\mathrm{T},2}$) distribution, correcting for bin migration on both the leading and subleading jets. A separate response matrix is generated for each centrality selection in Pb+Pb collisions as well as pp collisions in order to properly model the centrality dependence in the response. The response matrix contains the relationship between truth ($p_{\mathrm{T},1}$,$p_{\mathrm{T},2}$) and reconstructed ($p_{\mathrm{T},1}$,$p_{\mathrm{T},2}$). It is populated with the leading and subleading truth jets in an event, matched to their corresponding reconstructed jets within a $\Delta R < 0.3$, the reconstructed jets are not required to have the highest reconstructed p_{T} in the event. The response matrix is populated symmetrically in both $p_{\mathrm{T},1}$and $p_{\mathrm{T},2}$, using a weighting function so that the prior better represents the measured data. The number of iterations in the unfolding was chosen to have a stable result with respect to the number of iterations while minimizing the amplification of statistical uncertainties. Five iterations are used in the 0–10% central collisions, and four iterations are used in all other cases. The unfolded ($p_{\mathrm{T},1}$,$p_{\mathrm{T},2}$) distributions are projected to 1-dimensional x_{J} distributions in bins of $p_{\mathrm{T},1}$. In order to populate the x_{J} distribution down to 0.32 without introducing a large efficiency correction, the projection to x_{J} is done in bins of $p_{\mathrm{T},1} > 158$ GeV.

5 Systematic Uncertainties

This analysis considers two main categories of systematic uncertainties: the uncertainties associated with the jet measurement and those associated with the unfolding. The contribution to the systematic uncertainties from the combinatoric background subtraction is negligible and therefore not included. The uncertainties are applied to the jet response and propagated through the unfolding to the final x_{J} distributions.

The systematic uncertainty on the JES has four parts. First, there is a centrality-independent baseline component that is determined from *in situ* studies of the calorimeter response for jets reconstructed following the procedure used in 13 TeV pp collisions [22, 23]. The second, is a centrality-independent component accounting for the relative energy scale difference between the jet reconstruction procedures used in this note at 5 TeV and that used for 13 TeV pp collisions [24]. Potential inaccuracies in the MC sample in the description of the relative abundances of jets initiated by quarks and gluons and of the calorimetric response to quark and gluon jets are accounted for by the third component. The magnitude of this component was determined by comparing two generators, Pythia8 and Herwig7. The fourth, centrality-dependent, component accounts for a different structure and possibly a different detector response of jets in Pb+Pb collisions that is not modeled by the MC. The extent of this uncertainty is determined by the method used for 2015 and 2011 data [24] that compares calorimeter p_{T} and the sum of the transverse momentum of charged particles within the jet in data and MC samples. To account for the uncertainty on the JES in the dijet measurement, each component is varied separately by ± 1 standard deviation in MC samples, applied as a function of p_{T} and η, and the response matrix is recomputed. The data are then unfolded with the modified matrices.

The uncertainty due to the JER is evaluated by repeating the unfolding procedure with modified response matrices, where an additional contribution is added to the resolution of the reconstructed p_{T} using a Gaussian smearing procedure. The smearing factor is evaluated using an *in situ* technique in 13 TeV pp data that involves studies of dijet energy balance [25, 26] with additional contributions accounting for differences in calibration procedures for jet used in this analysis and those from 13 TeV pp data. Further, uncertainty is included to account for differences between the reconstruction used in this measurement and the jet reconstruction used in analyses of 13 TeV pp data. The resulting uncertainty from the JER is symmetrized.

The uncertainty on the unfolding procedure has three sources. The first source is the sensitivity to the prior. This was evaluated by modifying the weighting function used to set the prior in the response matrix, following the variations applied in Ref. [6]. This resulted in the modification of the prior with respect to unweighted MC being reduced (increased) for central (mid-central) collisions. The alternate prior in the most peripheral collisions is based on the unweighted MC. The second source is the sensitivity in the unfolding result to the minimum reconstructed jet p_{T} used in the analysis. The nominal value is 44 GeV. This minimum jet reconstruction threshold was increased to 50 GeV and the analysis procedure was repeated, with the difference from the nominal result taken as the systematic uncertainty contribution. Finally, the non-closure of the analysis in MC taken as a systematic uncertainty. These three components are first symmetrized and then combined together in quadrature to determine the total unfolding systematic uncertainty contribution.

Examples of the systematic uncertainties are shown for 0–10% and 60–80% central Pb+Pb collisions and in pp collisions in Figure 3. The total uncertainties on the x_{J} distributions in central and mid-central events are driven approximately equally by the sensitivity to the unfolding as well as the JES- and JER-related

uncertainties. In peripheral Pb+Pb collisions and *pp* collisions the systematic uncertainties are driven by the jet-related uncertainties.

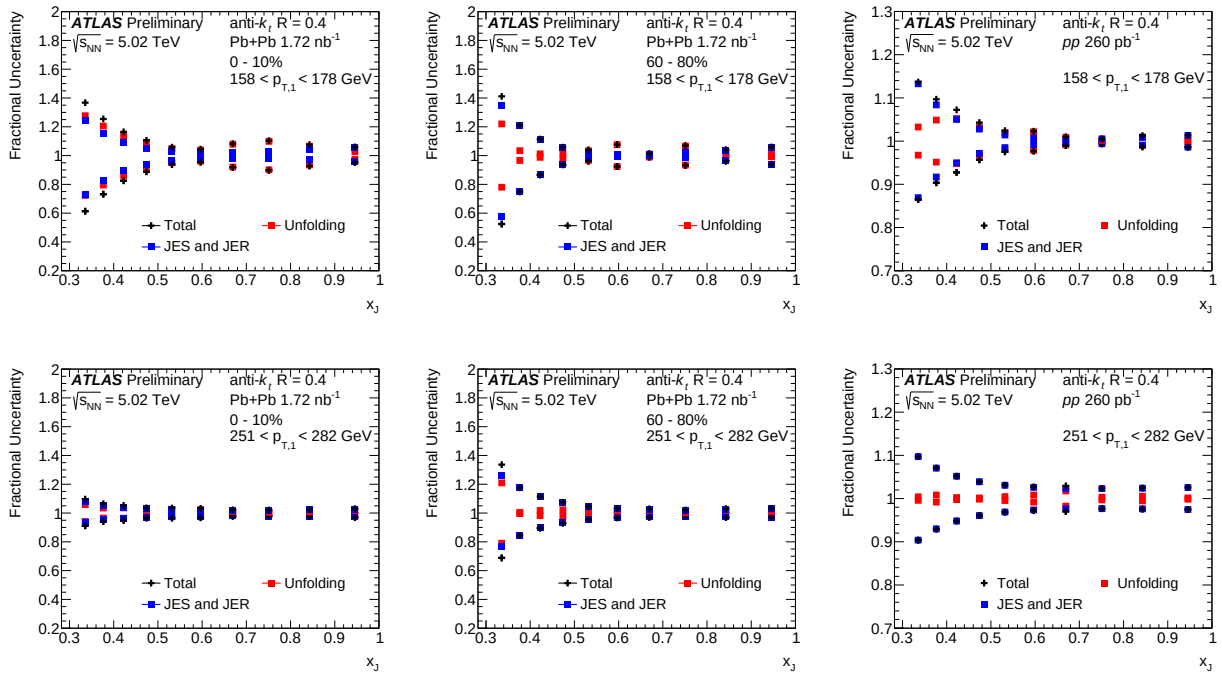

Figure 3: The systematic uncertainty contributions to the $\frac{1}{N_{pair}}\frac{dN_{pair}}{dx_J}$ distributions for $158 < p_{T,1} < 178$ GeV (top) and $251 < p_{T,1} < 282$ GeV (bottom) in 0–10% central Pb+Pb collisions (left), 60–80% central Pb+Pb collisions (middle), and *pp* collisions (right).

6 Results

The unfolded x_J distributions are presented over a rapidity interval of $|\eta| < 2.1$ and for leading jets in $p_{T,1}$ intervals between 158 GeV and 562 GeV. Figure 4 shows the x_J distributions for $158 < p_{T,1} < 562$ GeV in pp collisions. At low $p_{T,1}$ values, the x_J distributions increase approximately linearly with increasing x_J, and for $p_{T,1}$ >250 GeV the distributions become steeper for $x_J > 0.7$. The measurements are compared with the same distributions from PYTHIA8 and good agreement between the MC and the data is observed over the entire $p_{T,1}$ range of this measurement.

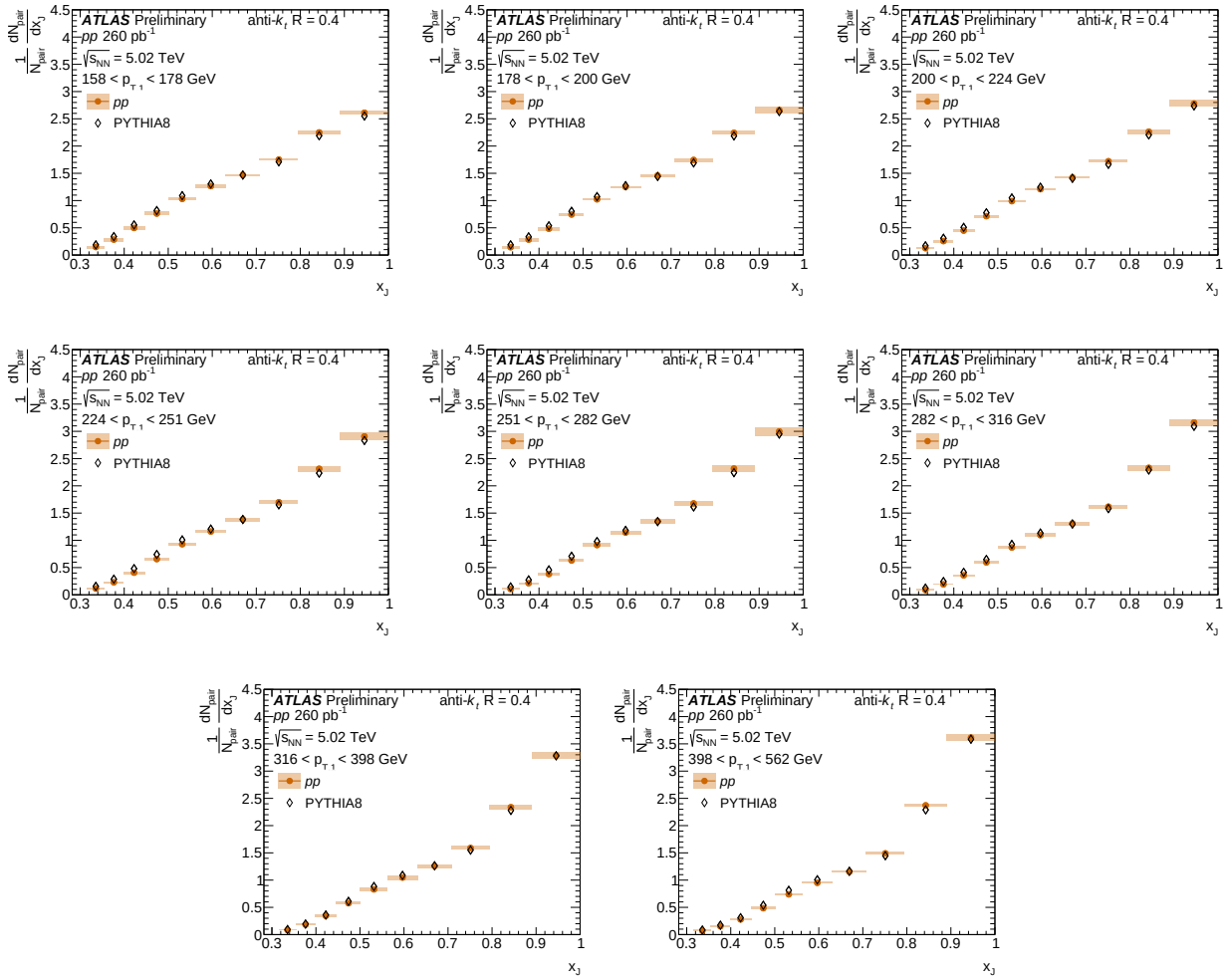

Figure 4: The x_J distributions in pp collisions (full markers) for the $p_{T,1}$ selections measured here. The error bars indicate the statistical uncertainties and are sometimes smaller than the points. The boxes show the systematic uncertainties. Values from PYTHIA8 are also shown (open diamond markers).

The unfolded x_J distributions for $R = 0.4$ jets for all Pb+Pb centrality selections and pp collisions are shown in Figure 5 for the same $p_{T,1}$ selections as in the previous figure. For all $p_{T,1}$ selections the modification of the x_J distributions in Pb+Pb collisions compared to pp collisions increases for more central collisions. For $158 < p_{T,1} < 178$ GeV the x_J distributions in the most central Pb+Pb collisions are consistent with a constant as a function of x_J for $x_J > 0.5$. For less central collisions and higher $p_{T,1}$ selections the x_J

distributions increase with increasing x_J. For $p_{T,1} < 224$ GeV, the x_J distributions in 60–80% Pb+Pb collisions are significantly different than those in pp collisions; however, for $224 < p_{T,1} < 282$ GeV the x_J distributions in peripheral Pb+Pb collisions are very similar to those in pp collisions (for $p_{T,1} > 282$ GeV there are not enough jets in the 60–80% centrality selection to perform the measurement).

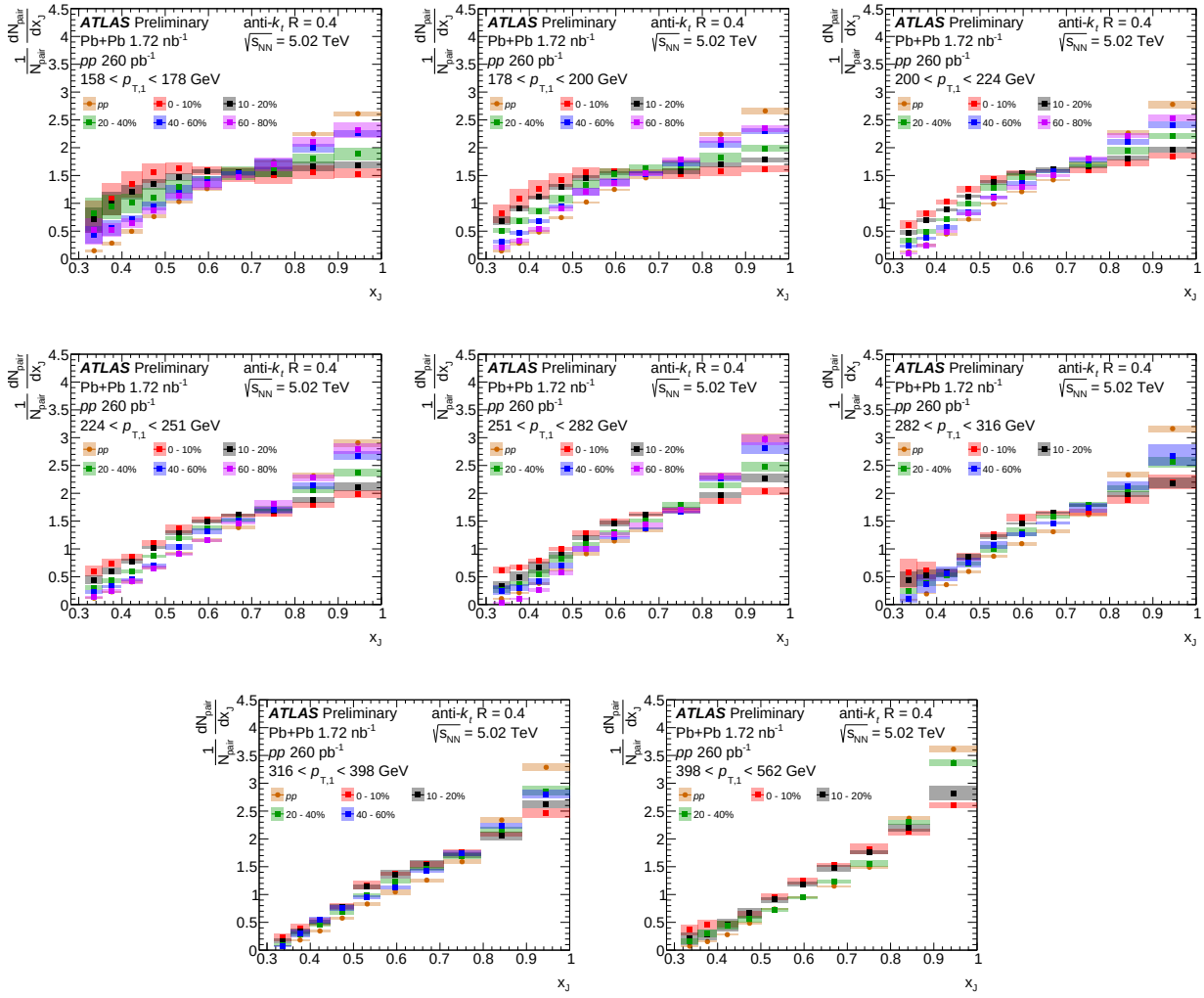

Figure 5: The x_J distributions for 0–10%, 10–20%, 20–40%, 40–60% and 60–80% centrality selections in Pb+Pb collisions compared to those in pp collisions. Each panel presents a different $p_{T,1}$ selection. The error bars, which are sometimes smaller than the points, show the statistical uncertainties and the boxes show the systematic uncertainties. At the higher values of $p_{T,1}$ some centrality classes are omitted from the plots because there are an insufficient number jets to perform the analysis.

In order to investigate the $p_{T,1}$ dependence of the x_J distributions, Figures 6 and 7 shows these distributions in 0–10% and 60–80% central Pb+Pb and pp collisions with the different $p_{T,1}$ selections overlaid. Qualitatively, both in Pb+Pb collisions and in pp collisions, the x_J distributions become steeper with increasing $p_{T,1}$. To more clearly see the $p_{T,1}$ dependence of the x_J distributions, Figure 8 shows the x_J distributions for the lowest and highest $p_{T,1}$ selections in both 0–10% central Pb+Pb collisions and pp collisions. The shape of the x_J distribution for $158 < p_{T,1} < 178$ GeV in the most central Pb+Pb collisions are qualitatively different from both pp collisions and the higher $p_{T,1}$ selection in the same centrality of Pb+Pb collisions. For the

higher $p_{\mathrm{T},1}$ selection, the distribution in pp collisions has approximately a 40% higher probability to have pairs with x_{J} between 0.9 and 1.0 than at the lower $p_{\mathrm{T},1}$ selection.

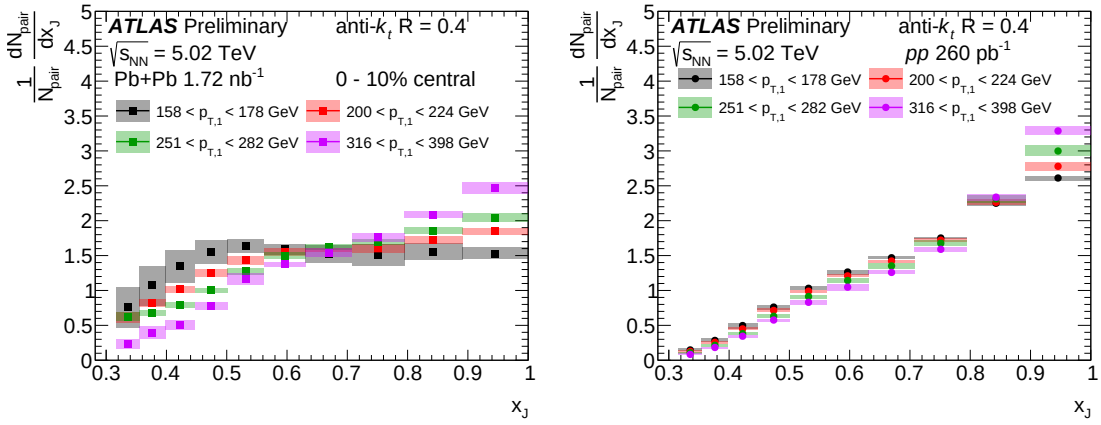

Figure 6: The x_{J} distributions in 0–10% central Pb+Pb collisions (left) and pp collisions (right) for different $p_{\mathrm{T},1}$ selections. The error bars, which are sometimes smaller than the points, show the statistical uncertainties and the boxes show the systematic uncertainties.

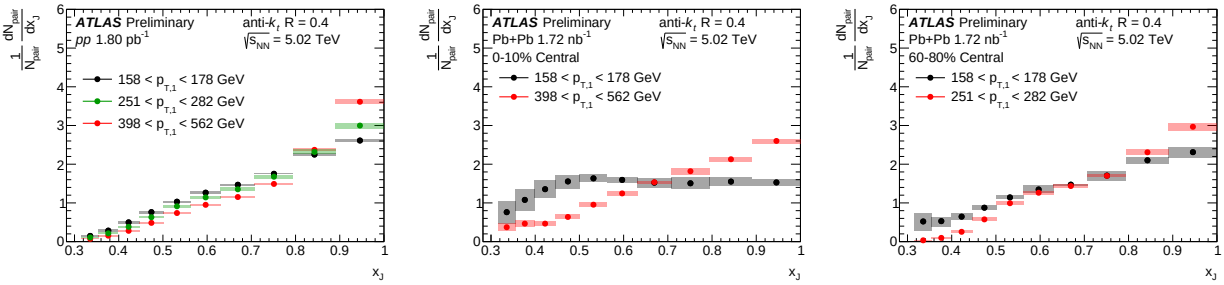

Figure 7: The left panel shows a comparison of the x_{J} distributions across three $p_{\mathrm{T},1}$ bins in pp collisions. The center (right) panel shows the comparison across two $p_{\mathrm{T},1}$ bins in 0 − 10% (60 − 80%) Pb+Pb collisions. Note that the higher $p_{\mathrm{T},1}$ range shown for the 60–80% central collisions is lower than what is shown for 0–10% central collisions.

The collision energy dependence of the x_{J} distributions is interesting for a number of reasons. First, the momentum fractions of the incoming nucleons carried by the quarks and gluons which undergo the hard scattering should be different at the two collision energies with more gluon jets at the higher collision energy. Second, the initial (prior to quenching) x_{J} distributions are different at the two collision energies due to differences in the jet momentum spectra and the larger expected contribution to multi-jet events at the higher collision energy. Finally, the QGP in Pb+Pb collisions at 5.02 TeV is expected to have a higher temperature than at 2.76 TeV. The first and second reasons for differences would be present in both pp and Pb+Pb collisions, while the third is related only to Pb+Pb collisions. Figure 9 shows the comparison of the x_{J} distributions in this measurement at $\sqrt{s_{\mathrm{NN}}}$ = 5.02 TeV to the same measurement at $\sqrt{s_{\mathrm{NN}}}$ = 2.76 TeV [6] for both pp collisions and the most central Pb+Pb collisions. Due to the smaller available luminosity at 2.76 TeV, this comparison is only possible for $p_{\mathrm{T},1} < 200$ GeV. The 5.02 TeV result has two $p_{\mathrm{T},1}$ selections (158–178 GeV and 178–200 GeV) that cover the range of the single $p_{\mathrm{T},1}$ selection for the 2.76 TeV measurement that overlaps with the 5.02 TeV measurement range. In pp collisions, the x_{J}

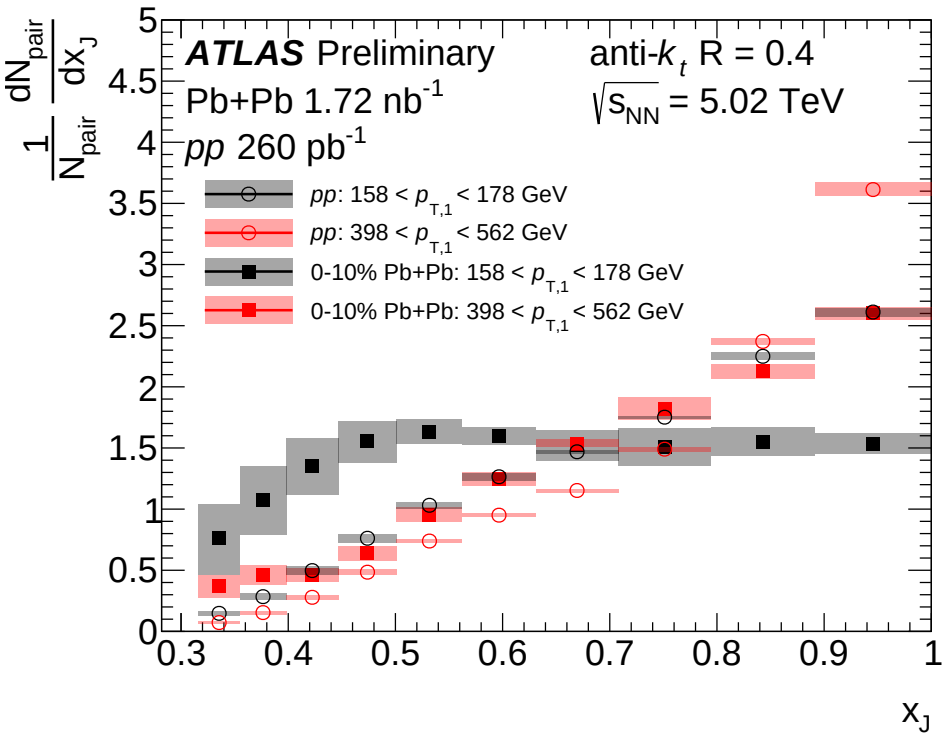

Figure 8: The x_J distributions in 0–10% central Pb+Pb and pp collisions for different $p_{T,1}$ selections. The error bars, which are sometimes smaller than the points, show the statistical uncertainties and the boxes show the systematic uncertainties.

distribution is observed to be more peaked at high x_J at 2.76 TeV than at 5.02 TeV with an approximately 15% higher fraction of jets with x_J larger than 0.9 at the lower collision energy. In 0–10% central Pb+Pb collisions, no significant collision energy dependence is observed.

A comparison of the x_J distributions with a theoretical prediction is provided in Figure 10. The x_J distributions for pp, 0 – 10%, and 60 – 80% Pb+Pb collisions are compared to calculations using the LIDO energy loss model [27]. This calculation uses the PYTHIA8 4C tune [28] parton shower information to initialize the LIDO transport model. The LIDO transport model considers energy loss from both elastic interactions and path length dependent medium induced radiation. Momentum carried by soft partons is redistributed into the angular phase space using a simple model mimicking the hydrodynamic response. Additionally this calculation uses initial conditions from the TRENTo model [29] to initialize a 2+1D viscous hydrodynamic [30] simulation of the medium. Figure 10 shows that the baseline calculations for pp collisions, PYTHIA8 4C tune with CTEQ6L1 PDFs, over-predicts the contribution from balanced dijets, with an increasing over-prediction with increasing $p_{T,1}$. Figure 10 also shows comparisons to predictions using the LIDO transport model for two values of the QGP coupling parameter, μ, for 0–10% and 60–80% Pb+Pb collisions. These predictions qualitatively agree with this measurement for both event centrality intervals and across $p_{T,1}$ intervals, however for $p_{T,1} > 398$ GeV there is a clear over-prediction of the fraction of symmetric dijets in central collisions. The difference between x_J distributions calculated for two values of the in-medium coupling parameter μ ($\mu = 2\pi T$ and $\mu = 1.5\pi T$) is typically smaller than the uncertainties on the measured x_J distributions and it is therefore not possible to discriminate between the two calculations.

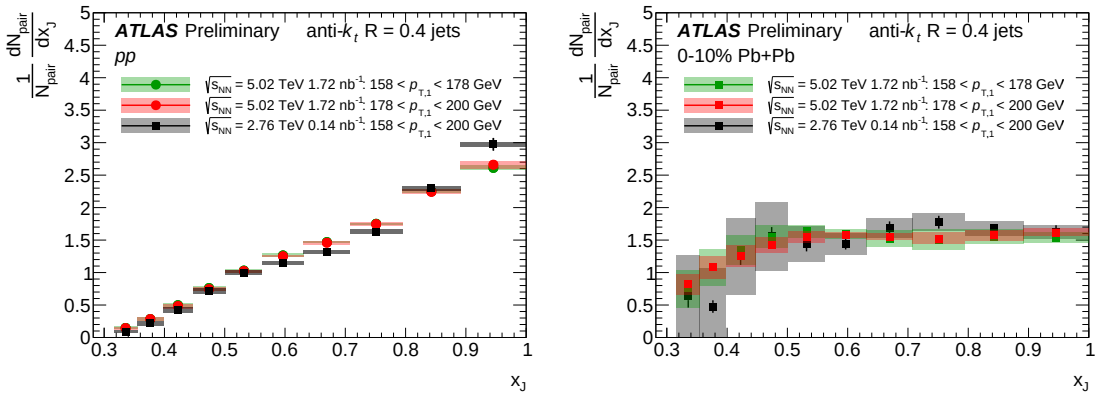

Figure 9: The x_J distributions in pp collisions (left) and 0–10% central Pb+Pb collisions (right) at 5.02 TeV compared the same distributions measured at 2.76 TeV from Ref. [6]. The 5.02 TeV results are shown for both $158 < p_{T,1} < 178$ GeV (green) and $178 < p_{T,1} < 200$ GeV (red) and the 2.76 TeV (black) results are shown for a single $p_{T,1}$ selection from 158–200 GeV.

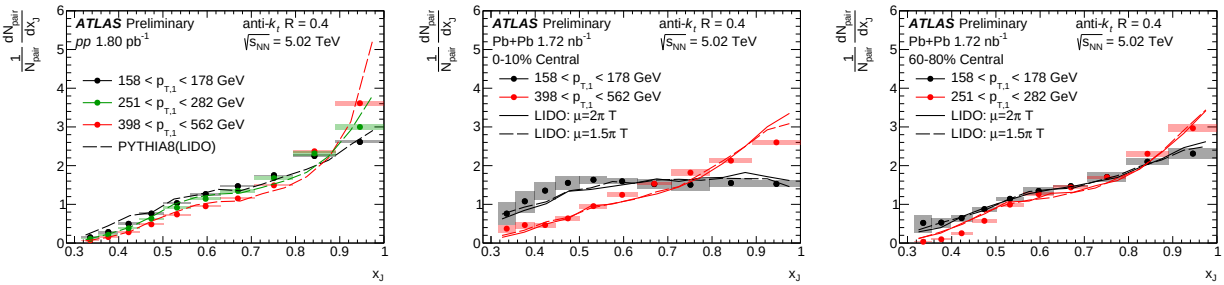

Figure 10: All panels shown comparisons of the x_J distributions to calculations using the LIDO transport model [27]. The left panel shows the comparison of their pp baseline to the measurement in pp collisions. The center (right) panel shows the comparison of the LIDO calculations in $0-10\%$ ($60-80\%$) Pb+Pb collisions for two variations of the QGP coupling parameter μ. Note that the higher $p_{T,1}$ range shown for the 60–80% central collisions is lower than what is shown for 0–10% central collisions.

7 Conclusions

This note presents a measurement of the differential dijet momentum balance, x_J, in both Pb+Pb and pp collisions at $\sqrt{s_{NN}}$ = 5.02 TeV. The measurement was performed differentially in the leading jet transverse momentum, $p_{T,1}$, and Pb+Pb collision centrality. The results are unfolded to correct for detector resolution. The resulting distributions show that across all $p_{T,1}$ ranges considered here, from 158 GeV to 562 GeV, significant broadening of the transverse momentum balance of back-to-back dijet pairs is observed in central Pb+Pb collisions with respect to pp collisions. The largest broadening is observed for $158 < p_{T,1} < 178$ GeV, where in central collisions the x_J distribution is consistent with flat for $x_J > 0.5$. The modifications observed in Pb+Pb collisions decrease toward more peripheral events. For the lowest $p_{T,1}$, slight modifications from pp are observed even for the 60–80% centrality Pb+Pb collisions. At higher transverse momenta, the modifications to the x_J distributions become smaller, and the results approach those seen for pp collisions. In the most central Pb+Pb collisions, the x_J distributions remain significantly

different than those in pp collisions up to $398 < p_{\mathrm{T},1} < 562$ GeV. Additionally, for $p_{\mathrm{T},1} < 200$ GeV, this measurement is found to be consistent with the 2.76 TeV Pb+Pb measurement [6]. These measurements will provide new information about the strength and path length dependence to jet quenching within the quark-gluon plasma.

References

[1] W. Busza, K. Rajagopal and W. van der Schee, *Heavy Ion Collisions: The Big Picture, and the Big Questions*, Ann. Rev. Nucl. Part. Sci. **68** (2018) 339, arXiv: 1802.04801 [hep-ph] (cit. on p. 2).

[2] ATLAS Collaboration, *Measurement of the nuclear modification factor for inclusive jets in Pb+Pb collisions at* $\sqrt{s_{\mathrm{NN}}}$ = 5.02 *TeV with the ATLAS detector*, Phys. Lett. **B790** (2019) 108, arXiv: 1805.05635 [nucl-ex] (cit. on pp. 2, 4).

[3] I. Vitev and B.-W. Zhang, *Jet tomography of high-energy nucleus-nucleus collisions at next-to-leading order*, Phys. Rev. Lett. **104** (2010) 132001, arXiv: 0910.1090 [hep-ph] (cit. on p. 2).

[4] ATLAS Collaboration, *Observation of a Centrality-Dependent Dijet Asymmetry in Lead-Lead Collisions at* $\sqrt{s_{NN}}$ = 2.77 *TeV with the ATLAS Detector at the LHC*, Phys. Rev. Lett. **105** (2010) 252303, arXiv: 1011.6182 [hep-ex] (cit. on p. 2).

[5] CMS Collaboration, *Observation and studies of jet quenching in PbPb collisions at nucleon-nucleon center-of-mass energy = 2.76 TeV*, Phys. Rev. **C84** (2011) 024906, arXiv: 1102.1957 [nucl-ex] (cit. on p. 2).

[6] ATLAS Collaboration, *Measurement of jet* p_{T} *correlations in Pb+Pb and pp collisions at* $\sqrt{s_{\mathrm{NN}}}$ = *2.76 TeV with the ATLAS detector*, Phys. Lett. **B774** (2017) 379, arXiv: 1706.09363 [hep-ex] (cit. on pp. 2, 6, 10, 12, 13).

[7] G.-Y. Qin and B. Müller, *Explanation of Dijet Asymmetry in Pb-Pb Collisions at the Large Hadron Collider*, Physical Review Letters **106** (2011), ISSN: 1079-7114, URL: http://dx.doi.org/10.1103/PhysRevLett.106.162302 (cit. on p. 2).

[8] M. Cacciari, G. P. Salam and G. Soyez, *The anti-*k_t *jet clustering algorithm*, JHEP **04** (2008) 063, arXiv: 0802.1189 [hep-ph] (cit. on pp. 2, 4).

[9] ATLAS Collaboration, *The ATLAS Experiment at the CERN Large Hadron Collider*, JINST **3** (2008) S08003 (cit. on p. 3).

[10] ATLAS Collaboration, *Trigger Menu in 2018*, ATL-DAQ-PUB-2019-001, 2019, URL: https://cds.cern.ch/record/2693402 (cit. on p. 3).

[11] ATLAS Collaboration, *Measurement of longitudinal flow decorrelations in Pb+Pb collisions at* $\sqrt{s_{NN}}$ = 2.76 *and 5.02 TeV with the ATLAS detector*, Eur. Phys. J. **C78** (2018) 142, arXiv: 1709.02301 [nucl-ex] (cit. on p. 3).

[12] T. Sjöstrand et al., *An Introduction to PYTHIA 8.2*, Comput. Phys. Commun. **191** (2015) 159, arXiv: 1410.3012 [hep-ph] (cit. on p. 4).

[13] ATLAS Collaboration, ATLAS-PHYS-PUB-2014-021, https://cds.cern.ch/record/1966419 (cit. on p. 4).

[14] R. D. Ball et al., *Parton distributions with LHC data*, Nucl. Phys. B **867** (2013) 244, arXiv: 1207.1303 [hep-ph] (cit. on p. 4).

[15] ATLAS Collaboration, *The Pythia 8 A3 tune description of ATLAS minimum bias and inelastic measurements incorporating the Donnachie–Landshoff diffractive model*, ATL-PHYS-PUB-2016-017, 2016, URL: https://cds.cern.ch/record/2206965 (cit. on p. 4).

[16] S. Agostinelli et al., *GEANT4—a simulation toolkit*, Nucl. Instrum. Meth. A **506** (2003) 250 (cit. on p. 4).

[17] ATLAS Collaboration, *The ATLAS Simulation Infrastructure*, Eur. Phys. J. C **70** (2010) 823, arXiv: 1005.4568 [physics.ins-det] (cit. on p. 4).

[18] M. Cacciari, G. P. Salam and G. Soyez, *FastJet user manual*, Eur.Phys.J. **C72** (2012) 1896, arXiv: 1111.6097 [hep-ph] (cit. on p. 4).

[19] ATLAS Collaboration, *Measurement of the azimuthal anisotropy of charged particles produced in $\sqrt{s_{NN}} = 5.02$ TeV Pb+Pb collisions with the ATLAS detector*, Eur. Phys. J. **C78** (2018) 997, arXiv: 1808.03951 [nucl-ex] (cit. on p. 4).

[20] G. D'Agostini, *A Multidimensional unfolding method based on Bayes' theorem*, Nucl. Instrum. Meth. **A362** (1995) 487 (cit. on p. 5).

[21] T. Adye, 'Unfolding algorithms and tests using RooUnfold', *Proceedings, PHYSTAT 2011 Workshop on Statistical Issues Related to Discovery Claims in Search Experiments and Unfolding, CERN,Geneva, Switzerland 17-20 January 2011*, CERN, CERN, 2011 313, arXiv: 1105.1160 [physics.data-an] (cit. on p. 5).

[22] ATLAS Collaboration, *Jet energy measurement with the ATLAS detector in proton-proton collisions at $\sqrt{s} = 7$ TeV*, Eur. Phys. J. C **73** (2013) 2304, arXiv: 1112.6426 [hep-ex] (cit. on p. 6).

[23] ATLAS Collaboration, *Jet energy scale measurements and their systematic uncertainties in proton-proton collisions at $\sqrt{s} = 13$ TeV with the ATLAS detector*, Phys. Rev. D **96** (2017) 072002, arXiv: 1703.09665 [hep-ex] (cit. on p. 6).

[24] ATLAS Collaboration, *Jet energy scale and its uncertainty for jets reconstructed using the ATLAS heavy ion jet algorithm*, ATLAS-CONF-2015-016 (2015), URL: https://cds.cern.ch/record/2008677 (cit. on p. 6).

[25] ATLAS Collaboration, *Jet energy resolution in proton-proton collisions at $\sqrt{s} = 7$ TeV recorded in 2010 with the ATLAS detector*, Eur. Phys. J. C **73** (2013) 2306, arXiv: 1210.6210 [hep-ex] (cit. on p. 6).

[26] ATLAS Collaboration, *Determination of jet calibration and energy resolution in proton-proton collisions at $\sqrt{s} = 8$ TeV using the ATLAS detector*, (2019), arXiv: 1910.04482 [hep-ex] (cit. on p. 6).

[27] W. Ke, Y. Xu and S. A. Bass, *Modified Boltzmann approach for modeling the splitting vertices induced by the hot QCD medium in the deep Landau-Pomeranchuk-Migdal region*, Phys. Rev. C **100** (6 2019) 064911, URL: https://link.aps.org/doi/10.1103/PhysRevC.100.064911 (cit. on pp. 11, 12).

[28] R. Corke and T. Sjöstrand, *Interleaved parton showers and tuning prospects*, Journal of High Energy Physics **2011** (2011), ISSN: 1029-8479, URL: http://dx.doi.org/10.1007/JHEP03(2011)032 (cit. on p. 11).

[29] J. S. Moreland, J. E. Bernhard and S. A. Bass, *Alternative ansatz to wounded nucleon and binary collision scaling in high-energy nuclear collisions*, Phys. Rev. C **92** (1 2015) 011901, URL: https://link.aps.org/doi/10.1103/PhysRevC.92.011901 (cit. on p. 11).

[30] H. Song and U. Heinz, *Causal viscous hydrodynamics in 2 + 1 dimensions for relativistic heavy-ion collisions*, Phys. Rev. C **77** (6 2008) 064901, URL: https://link.aps.org/doi/10.1103/PhysRevC.77.064901 (cit. on p. 11).